Kirigami-Inspired Structures for Smart Adhesion

Doh-Gyu Hwang, Katie Trent, and Michael D. Bartlett*

Department of Materials Science and Engineering, Soft Materials and Structures Lab, Iowa State University of Science and Technology, 528 Bissell Rd, Ames, Iowa 50011, United States

Ⓢ Supporting Information

ABSTRACT: Spatially controlled layouts of elasticity can provide enhanced adhesion over homogeneous systems. Emerging techniques in kirigami, where designed cuts in materials impart highly tunable stiffness and geometry, offer an intriguing approach to create well-defined layouts of prescribed elastic regions. Here, we show that kirigami-inspired structures at interfaces provide a new mechanism to spatially control and enhance adhesion strength while providing directional characteristics for smart interfaces. We use kirigami-inspired cuts to define stiff and compliant regions, where above a critical, material-defined length scale, bending rigidity and contact width can be tuned to enhance adhesive force capacity by a factor of ∼100 across a spatially patterned adhesive sheet. The directional nature of these designs also imparts anisotropic responses, where peeling in different directions results in anisotropic adhesion ratios of ∼10. Experimental results are well-supported by theoretical predictions in which the bending rigidity and contact width of kirigami-inspired structures and interconnects control the adhesive capacity. These new interfacial structures and design criteria provide diverse routes for advanced adhesive functionality, including spatially controlled systems, wearable kirigami-inspired electronics, and anisotropic kirigami-inspired bandages that enable strong adhesive capacity while maintaining easy release.

KEYWORDS: tunable adhesion, kirigami, dry adhesive, interface, fracture, crack trapping
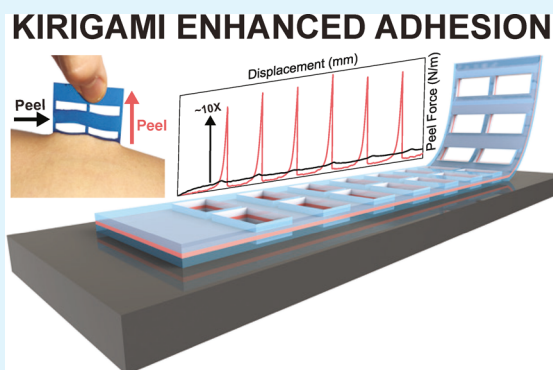
■ INTRODUCTION

The art of paper cutting, often known as kirigami and jiǎnzhǐ, can be applied to engineer materials with unique functional properties such as elastic softening, high extensibility, and the creation of complex 3D morphologies, through designed cuts.[1−5] This approach has been implemented to enhance the functionality of diverse material sets, leading to a spectrum of smart electronics and sensors.[6−12] Although there have been many reports on the mechanical behavior of kirigami structures and their potential functional applications, the influence of incisions or the complete removal of film materials at interfaces has not been well-explored. With the ability to tune mechanics and structure through cuts, kirigami-inspired designs offer a great potential to control adhesion and wetting through the precise control of interfacial properties.

Controlled and tunable adhesion is critical to a number of applications including biomedical systems, robotics, and manufacturing.[13−21] Conventionally, pressure-sensitive adhesives have been used to achieve high adhesive strength across an interface.[22] Although significant enhancement in adhesion can be attained through viscoelasticity,[23] these types of adhesives often display low reversibility, can leave behind undesirable residues through cohesive failure, and are particularly susceptible to degradation by particulate contamination. To overcome these constraints, works on reversible adhesives have focused on tuning interfacial geometry and elastic properties of materials. For example, micropillar arrays

and carbon nanotubes with various tip geometries and aspect ratios have been studied to control the adhesive strength.[24−28] Adhesion control in these systems is typically associated with contact splitting mechanisms, where crack reinitiation, tunable stress concentrations, and adaptability to surfaces can lead to enhanced adhesion strength.[29−31] Although microstructured surfaces have been well-demonstrated to control adhesion, specialized equipment, complex procedures, and additional fabrication steps are typically required to achieve desirable performance.

In addition to fibrillar features, reversible adhesives have been developed by controlling the interfacial structure and stiffness. Interfacial structures such as directional discontinuities and wrinkles in elastomeric substrates have demonstrated the ability to alter crack paths when cracks encounter prescribed patterns.[32−35] Embedding surface microchannels filled with liquid or air enhance adhesion through dissipative effects when propagating cracks become trapped at the channels.[36,37] Controlling interfacial stiffness by integrating rigid fabrics into soft elastomers enables adhesives to create intimate contact over large areas, while maintaining stiffness to minimize strain energy and achieve high loads.[38,39] Patterning interfacial elasticity can allow for tunable adhesion, where changes in

interfacial stiffness can allow for control of crack dynamics. This has been investigated through discrete regions of patterned stiffness across an interface, where the adhesion force can be tuned at stiffness transitions.[40,41] Although these studies investigated patterned rigidity, they focused on discrete patterns without interconnects and film continuity commonly observed in kirigami designs. All of the above-mentioned techniques have utilized interfacial structures to improve adhesive properties. However, systematic layouts of continuous films patterned by cuts, as seen in recent exploration of kirigami for engineering design, have been unexplored.

Here, we show that kirigami-inspired structures at interfaces provide a mechanism to spatially control and enhance adhesion strength while providing directional characteristics for high-capacity, easy-release interfaces. Kirigami-inspired adhesives are created by introducing cuts through rapid laser machining into continuous adhesive films consisting of elastomeric interfaces supported by inextensible films. Although cutting films has been utilized in various art forms, we choose to describe the presented patterns as kirigami-inspired as we utilize repeating cut patterns in continuous films with interconnected structures, which are the characteristics of the kirigami design. We study the peel adhesion response of these systems by varying the interconnect structure and interfacial geometry. This approach introduces spatially varying regions of stiff and compliant regions which allow for the systematic tuning of bending rigidity and actual contact width. As cracks propagate through these regions, a material-defined characteristic length scale is found to dictate force enhancement, where above a critical length both bending rigidity and actual contact width can be tuned in stiff and compliant regions to enhance adhesive force capacity by a factor of ~100 across a sheet. The influence of interconnects on adhesion is further investigated, and as the number on interconnects increases, the adhesive force decreases and approaches that of a homogeneous strip as the bending rigidity contrast between stiff and compliant regions decreases. Furthermore, we demonstrate the anisotropic properties of kirigami-inspired adhesives, where peeling along orthogonal directions results in anisotropic adhesive ratios of ~10. These experimental results are supported by theoretical predictions in which the bending rigidity and actual contact width of kirigami-inspired interconnects and structures are found to drive the adhesive capacity. This model well describes the experimental data and provides general design criteria for diverse kirigami-inspired adhesive structures. These structures and design criteria open new possibilities for advanced adhesive functionality, including spatially controlled systems, wearable electronics, and anisotropic bandages that enable strong adhesive capacity and easy release, which we demonstrate with a skin-mounted kirigami-inspired adhesive strip.

■ RESULTS AND DISCUSSION

Three different adhesive designs are created to investigate the effect of kirigami-inspired structures on peel adhesion (Figure 1a−c). Each design consists of alternating stiff and compliant regions of equal thickness, which are made of an adhesive layer and encapsulation layer of polydimethylsiloxane (PDMS) (E = 880 ± 40 kPa) separated by an inextensible polyethylene terephthalate (PET) strip (E = 2.6 ± 0.1 GPa). In both regions, PDMS serves as the adhesive layer. Model A consists of alternating sections of discrete stiff and compliant regions, where the PET sheet is absent in the compliant region. Model B introduces stiff interconnects, which bridge across the
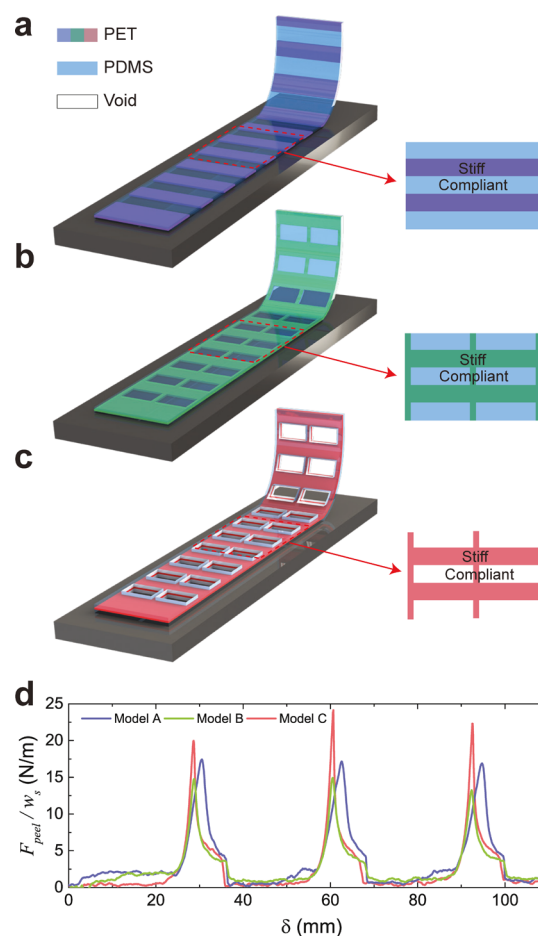
Figure 1. (a−c) Schematics of kirigami-inspired adhesives, which consist of alternating stiff and compliant regions, under 90° peel loading. (a) Compliant region of model A is continuous, whereas (b) model B incorporates rigid interconnects on the continuous layer and (c) model C consists of interconnects supported by an adhesive with voids between interconnects. (d) A representative normalized peel force vs displacement plot for each model.

compliant regions to connect the stiff regions. Model C is designed by eliminating the PDMS regions between interconnects in the compliant regions, creating an open structure. Initially, there are three interconnects, one at each edge and another in the center of the strip. The adhesive strips are examined with 90° peel adhesion measurements, where the interfacial crack propagates through the alternating compliant/stiff regions.

Figure 1d shows representative normalized peel force—displacement curves for each model. Although the geometry of the stiff region is identical in all three models, the addition of interconnects (model B) or further removal of PDMS in the compliant region (model C) influences the peak force. Relative to model A, the average peak force achieved in model B decreases by over 15%, whereas the average peak force in model C increases by over 30%. The structure of the interface is also observed to alter the crack propagation behavior. In Figure 2b, we plot the relative displacement $\delta_{relative}$ of the peel front versus the absolute displacement δ of the substrate, where $\delta_{relative}$ is the distance between the position of the peel line on the kirigami-inspired adhesive and a homogenous adhesive (see Figure S1 for images). Initially, $\delta_{relative}$ = 0 for all models; however, as the peel line reaches the stiff region the crack
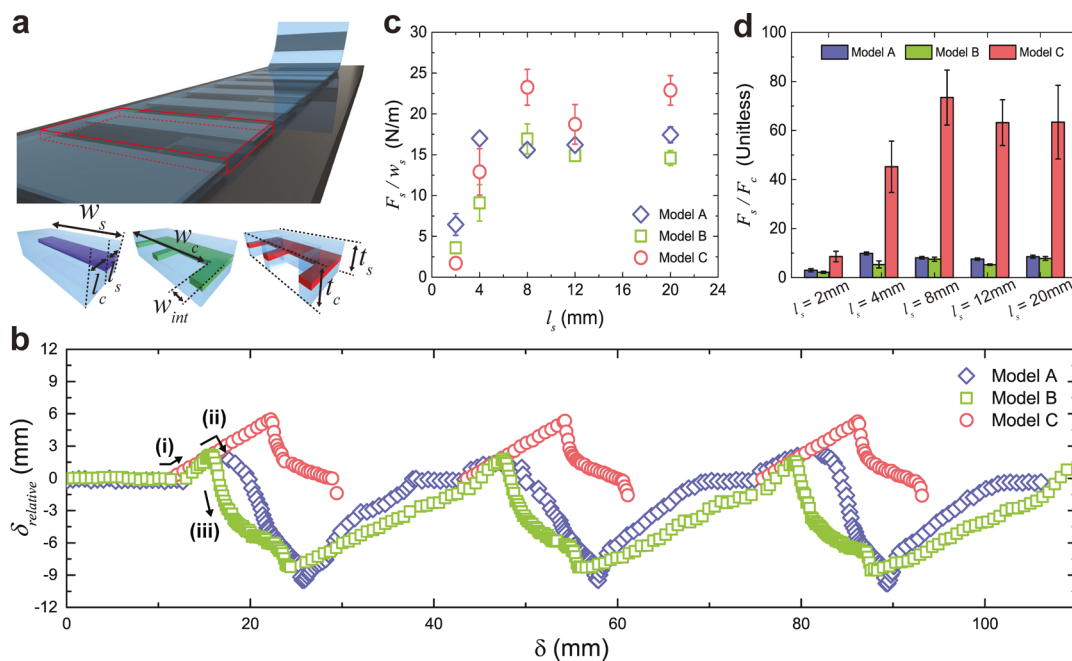
Figure 2. (a) Schematics of a kirigami-inspired adhesive with geometric parameters and different designs. For models A and B, $w_c = w_s$, while the voids between interconnects in model C results in $w_{c,modelC}$ being equal to the sum of the widths of individual interconnects w_{int} such that $w_{c,model\ C} = \sum_{j=1}^{N} w_{int,j}$, where N is the number of interconnects in the compliant region ($N = 3$ and $w_{int} = 2$ mm for the data presented in the figure). (b) Plot of relative displacement ($\delta_{relative}$) of the three adhesive models vs substrate displacement (δ). $\delta_{relative}$ is measured with respect to the position of the peel front of a homogeneous adhesive. Data points below zero in model C are absent because of the void areas when the peel front crosses the compliant interface. (c) Plot of normalized peak force of each model vs length of the stiff region l_s. (d) Bar chart illustrating the adhesion enhancement ratio (F_s/F_c) as a function of l_s.

decelerates, as demonstrated by an increase in $\delta_{relative}$, and gets trapped at the stiff interface (zone i and ii in Figure 2b). Further displacement results in sudden interfacial failure, where the crack is accelerated and $\delta_{relative}$ decreases (zone iii in Figure 2b). Here, we see that model C shows the most significant crack trapping, as the crack not only approaches a discontinuity in stiffness but must also reinitiate at the stiff interface.

To quantitatively explain the adhesion enhancement of kirigami-inspired adhesives, we follow a fracture mechanics energy balance approach. For a homogeneous adhesive strip under 90° peel loading, the crack propagates with a steady-state peel force with $F_{peel} = wG_c$, where w is the strip width and G_c is the critical strain energy release rate for the interfacial fracture.[42] However, for a heterogeneous strip, the peel force in the compliant region (F_c) and stiff region (F_s) varies as the crack propagates into the interface between these regions. This interface modifies the shape of the bent adhesive strip, which changes the mechanical energy in the system.[40,43] The change in shape depends on the bending rigidity (EI) of the two regions, where E is the elastic modulus and I is the second moment of area. Additionally, for the case of kirigami-inspired adhesives, the actual contact width changes as the crack travels across the interface from w_c to w_s. In this framework, the effective adhesion enhancement ratio of the peel force is calculated by considering the variation of total energy such that

$$\frac{F_s}{F_c} = \frac{E_s I_s w_s}{E_c I_c w_c} \tag{1}$$

where the subscripts s and c denote the stiff and compliant terms, respectively. Equation 1 shows that the enhancement ratio of kirigami-inspired adhesives is controlled by the

difference in bending stiffness EI and actual contact width w in both regions.

To optimally design kirigami-inspired adhesives, the relative size and geometry of the stiff and compliant regions need to be controlled. We consider the heterogeneous kirigami-inspired adhesive as a repeating array of unit cells with a compliant and a stiff region (Figure 2a). The stiff region is characterized by width w_s, length l_s, and thickness t_s, which consists of a PET sheet t_{PET} and two encapsulating PDMS layers t_{PDMS}. The width and thickness of the stiff region are constant throughout the experiment ($w_s = 46$ mm, $t_s = 0.75 \pm 0.1$ mm). The length $l_s = 2, 4, 8, 12,$ and 20 mm is selected based on the characteristic length of the stiff region ($l_{ch,s} = \sqrt{\frac{2E_s I_s}{w G_c}} \approx 6.4$ mm), where the characteristic length l_{ch} is a length scale comparable to the dimension of the stress field at the peel front.[43] If l_s is smaller than $l_{ch,s}$, the peel front propagates from a compliant region to a stiff region without fully undergoing the crack-arresting effect, which reduces adhesion enhancement. The compliant region is characterized by width w_c, length l_c, and thickness t_c in the same manner. The length and thickness of the compliant region are constant throughout the experiment ($l_c = 12$ mm, $t_c = t_s$), where l_c is greater than the characteristic length of the compliant region ($l_{ch,c} = \sqrt{\frac{E_c I_c}{E_s I_s}} l_{ch,s} \approx 2$ mm).[43] The width w_c is constant for models A and B ($=46$ mm), whereas w_c varies in model C as $w_{c,modelC} = \sum_{j=1}^{N} w_{int,j}$, where N ($=3$) is the number of interconnects and w_{int} ($=2$ mm) is the interconnect width.

Figure 2c illustrates the normalized peak force of the stiff region for each model as a function of the length of the stiff region. In general, adhesives with shorter l_s ($=2, 4$ mm) than $l_{ch,s}$ in the stiff region show a reduced enhancement because the
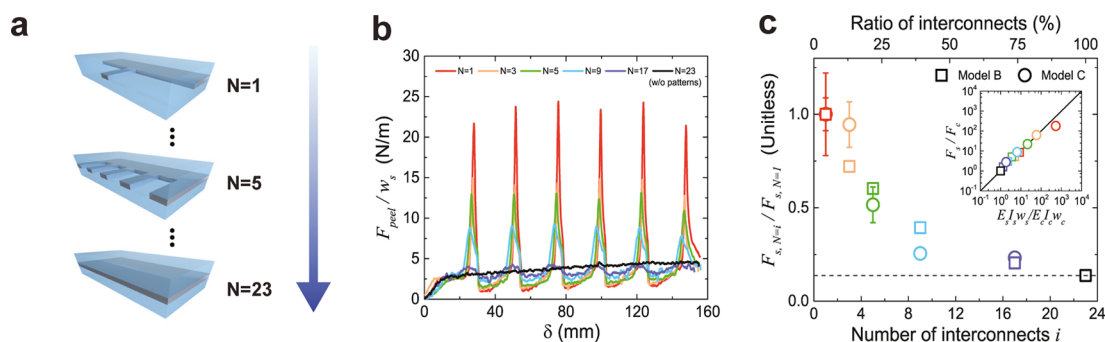
Figure 3. (a) Schematic diagram showing a varying number of interconnects in the compliant region. (b) Normalized peel force F_{peel}/w_s vs displacement plot for model B with varying number of interconnects. (c) Relative adhesion force of systems with multiple interconnects over a structure with a single interconnect ($F_{s,N=i}/F_{s,N=1}$) as a function of the number of interconnects. The black dashed line indicates the value of a homogeneous adhesive. The inset shows the adhesion enhancement ratio F_s/F_c as a function of $E_sI_sw_s/E_cI_cw_c$, where the colors match the legend in component b.
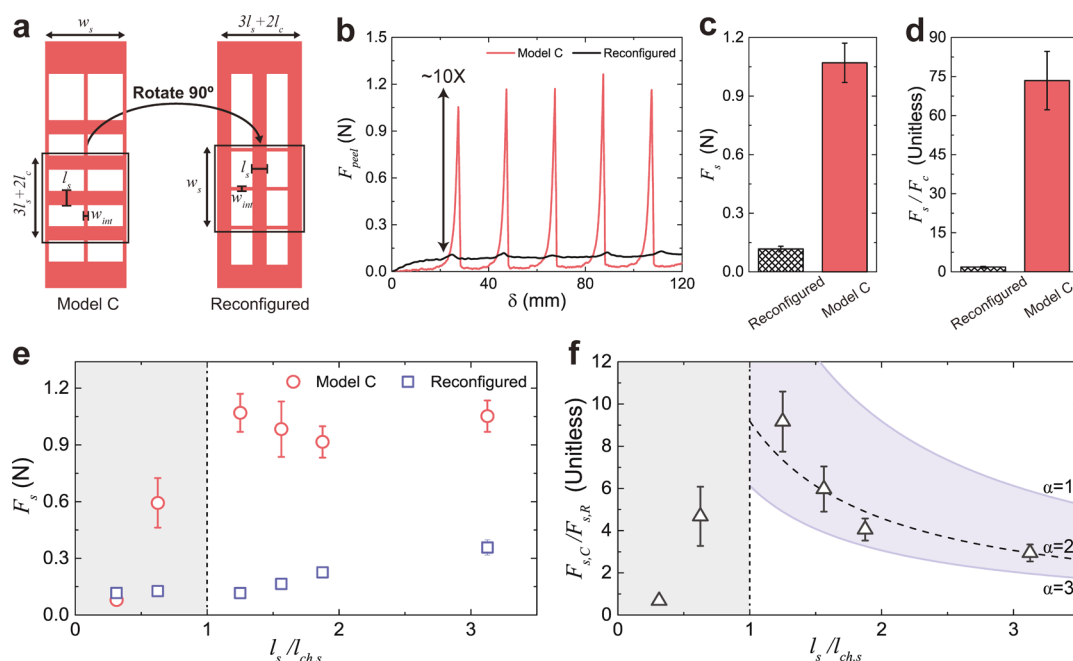
Figure 4. (a) Schematic diagram of a model C adhesive and a directionally reconfigured adhesive. (b) F_{peel} vs displacement plot for a model C and reconfigured adhesive. (c) F_s and (d) adhesion enhancement ratio (F_s/F_c) for model C and the reconfigured model. $l_s = 8$ mm for components a−d. (e) F_s vs $l_s/l_{ch,s}$, where l_s is varied from 2 to 20 mm. (f) Adhesion anisotropy ratio ($F_{s,C}/F_{s,R}$) vs $l_s/l_{ch,s}$, where the lines are the predictions from eq 2 with the specified α values and the blue shading represents the region within these limits. Gray regions in e and f represent regions, where $l_s/l_{ch,s} < 1$. All adhesives within the figure have three interconnects ($N = 3$).

peel front travels across the region with partial crack arrest. In contrast, the peak force is fully enhanced across a stiff interface for systems with larger l_s (=8, 12, 20 mm) than $l_{ch,s}$ in the stiff region, and the value is relatively constant regardless of the length of the stiff region. Figure 2d shows the adhesion enhancement ratio (F_s/F_c) obtained by dividing the peak force in the stiff region by the force in the compliant region. When model C meets the criterion $l_s > l_{ch,s}$, the adhesion enhancement ratio increases to 60−70, greatly exceeding other models. Importantly, the significant enhancement in model C is not only due to the variation in stiffness but also attributed to the reduced actual contact width in the compliant region. This influence is important for the design of kirigami-inspired adhesives, as cut geometries can be generated to tune adhesion through both heterogeneous stiffness and actual contact width, expanding design space beyond patterned stiffness alone.

The role of interconnects on adhesion enhancement is further investigated by varying the number (N) of interconnects between 1 and 23 (as illustrated in Figure 3a). The width of interconnects w_{int} (=2 mm) and the stiff region w_s (=46 mm) are constant throughout the experiments, and the patterned system is equal to a homogeneous adhesive when N = 23. The normalized peel force versus displacement plot in Figure 3b shows that as the number of interconnects increases, F_{peel}/w_s systematically decreases. When the adhesive strip becomes homogeneous ($N = 23$), the peel force becomes steady and no longer displays a spatially varying adhesive force. Figure 3c shows a plot of the normalized peak force with a varying number of interconnects ($F_{s,N=i}$) over that of a sample with a single interconnect ($F_{s,N=1}$) as a function of the number of interconnects. Here, we see that increasing the number of stiff interconnects in the compliant region results in reduced crack-trapping effects and a reduced peak adhesive force. This
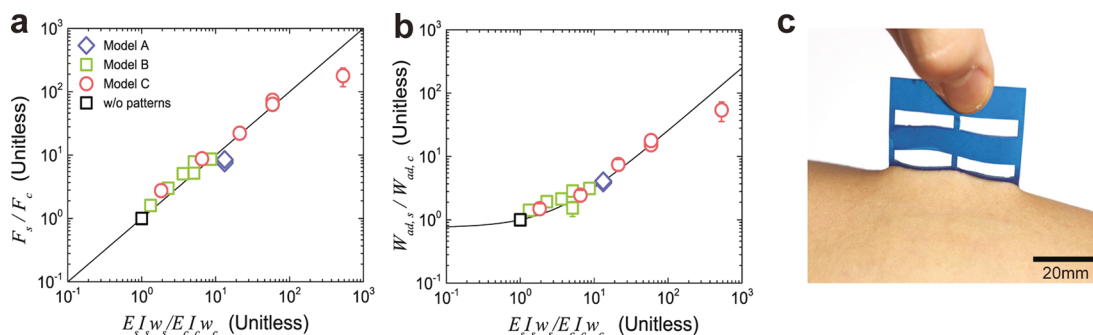
Figure 5. (a) log−log plot of the adhesion enhancement ratio (F_s/F_c) vs the contrast in bending stiffness and width ($E_sI_sw_s/E_cI_cw_c$), where the solid line is the prediction from eq 1. (b) log−log plot of the enhancement ratio in the work of adhesion vs $E_sI_sw_s/E_cI_cw_c$, the solid line is an empirical fit with $y = 1/4x + 3/4$. In both figures, data points that do not meet the length criterion $l_s > l_{ch,s}$ are excluded. (c) Photograph of a kirigami-inspired adhesive peeling off from an arm.

can be explained in the context of eq 1, where additional interconnects in the compliant region increase the bending rigidity, reducing the adhesion enhancement ratio (Figure 3c inset).

Owing to the directional nature of the kirigami structures, kirigami-inspired adhesives are expected to display anisotropic adhesive characteristics. This is investigated by selecting a unit cell in the model C design and rotating 90° with constant dimensions to create a reconfigured model (Figure 4a). Figure 4b shows a plot of the normalized peel force as a function of displacement for a model C adhesive and a directionally reconfigured adhesive ($l_s = 8$ mm and $w_{int} = 2$ mm). The average peak force of the model C design is ∼10× higher than that of the reconfigured model. Figure 4c,d summarizes these results by plotting the peak force F_s and the adhesion enhancement ratio F_s/F_c of the two directionally contrasting designs. It is shown that when cuts are perpendicular to the crack propagation direction, the peak force and enhancement ratio are high. Alternatively, the reconfigured model has cuts parallel to the crack propagation direction, resulting in a low peak force and enhancement ratio. This is due to two primary factors. First, model C meets the criterion $l_s > l_{ch,s}$, whereas the reconfigured design does not, resulting in enhanced crack trapping and adhesion enhancement for model C. Second, the actual contact width in the compliant region for model C is reduced, where $w_c = 0.13w_s$, whereas the reconfigured structure has $w_c = 0.50w_s$.

To design cut patterns for anisotropic adhesion, we consider the following criteria. For model C, $l_s \geq l_{ch,s}$ and $w_{int} \ll l_{ch,s}$; this will result in an increased $F_{s,C}$ and a decreased $F_{c,C}$, where we introduce the second subscript to denote the design. Upon reconfiguring model C (90° rotation), the slender interconnects from model C become the stiff regions in the reconfigured model, where because of the condition that $w_{int} < l_{ch,s}$, the crack will not be fully arrested and $F_{s,R}$ will be reduced. Further, the contact width at the stiff interface in the reconfigured model should be minimized while still allowing for crack arrest in model C, where we find that $l_{s,C} \simeq l_{ch,s}$. To quantify this effect, first we define the adhesion anisotropy ratio as $F_{s,C}/F_{s,R}$, where $F_{s,C}$ is the peak force in model C and $F_{s,R}$ is the peak force in the reconfigured model. Given the conditions above, the stiffness variation in the reconfigured model is reduced, and approximations are made such that $w_{s,R} = w_{c,R}$ and $F_{s,R} = \alpha F_{c,R}$, where α describes the magnitude of the crack arrest in the reconfigured model with $\alpha = 1$ representing a minimized crack-arresting response. Upon rearranging eq 1 to $F_{s,C} =$

$(E_sI_sw_s/E_cI_cw_c)F_{c,C}$ and substituting the respective F_s terms into the adhesion anisotropy ratio, we find that for $l_s \geq l_{ch,s}$

$$\frac{F_{s,C}}{F_{s,R}} = \frac{E_sI_sw_s}{E_cI_cL_s\alpha} \qquad (2)$$

where $L_s = \sum_{i=1}^{N_R} l_{s,i}$ and N_R is the number of rotated stiff segments in the reconfigured model. This shows that the adhesion anisotropy ratio is inversely proportional to l_s when $l_s \geq l_{ch,s}$, demonstrating that for maximum anisotropy ratios, l_s should be approximately equal to $l_{ch,s}$ to provide enhancement in model C while minimizing peel width during removal of the reconfigured model. This is experimentally examined by varying l_s across the range $0.31l_{ch,s} \leq l_s \leq 3.1l_{ch,s}$ for model C and the reconfigured model and measuring $F_{s,C}$ and $F_{s,R}$. As shown in Figure 4e, $F_{s,C}$ increases until $l_s/l_{ch,s} \simeq 1$ at which point $F_{s,C}$ reaches a plateau value, whereas $F_{s,R}$ increases throughout the $l_s/l_{ch,s}$ range as the peel width increases. Therefore, when looking at the adhesion anisotropy ratio ($F_{s,C}/F_{s,R}$) in Figure 4f, a maximum value is obtained when $l_s/l_{ch,s} \simeq 1$ and then decreases as l_s increases. When eq 2 is plotted with three different α values, the data is best described by $\alpha = 2$, demonstrating that the modest crack arrest occurs at the stiff regions in the reconfigured model. By further minimizing the crack arrest by decreasing w_{int}, the adhesion anisotropy ratio could be further enhanced. These experiments and analyses demonstrate that through designed layouts of elasticity and interconnects, kirigami-inspired adhesives with desired anisotropic properties can be created.

To examine the general behavior of kirigami-inspired adhesives relative to the theoretical predictions from eq 1, we plot the adhesion enhancement ratio (F_s/F_c) as a function of the bending stiffness and the width ratio ($E_sI_sw_s/E_cI_cw_c$) in Figure 5a. The plot shows an excellent agreement between the experimental data and eq 1 without any data-fitting parameters. When an adhesive is homogeneous, there is no enhancement in the peak force ($F_s = F_c$). In contrast, when a periodic layout of kirigami-inspired patterns is introduced onto the adhesive, periodic undulations of the peel force are observed ($F_s > F_c$). The adhesion enhancement ratio F_s/F_c of the kirigami-inspired adhesives varies by a factor of ∼100 relative to a homogeneous adhesive. For the case of models B and C, experimental data points are distributed along the prediction line, which depends on the number of interconnects in the compliant regions. The peak force F_s and the adhesion enhancement ratio F_s/F_c decrease with an increasing number of interconnects as the heterogeneous system becomes more similar to a homogeneous

strip (see Figure 3c inset for details). A deviation from this prediction is observed for model C with a single interconnect ($N = 1$), where the theory overpredicts the experimental value. We attribute this deviation to the poor load sharing across the single interconnect. These results provide a general design criteria for kirigami-inspired adhesives under peel loading, where further tuning of the interfacial structure such as changing thickness, interconnect geometry, or materials could lead to greater enhancements and control of the adhesion force.

We also compute the work of adhesion W_{ad} of kirigami-inspired adhesives, which represents the work done by an external loading system during the creation of new surfaces between the adhesive and the substrate.[44] The work of adhesion when a peel front crosses a stiff interface is given by calculating the area under the curve of a peel force–displacement plot such that $\frac{1}{w_s(\delta_p - \delta_0)} \int_{\delta_0}^{\delta_p} F(\delta)\, \mathrm{d}\delta$, where δ_0 is the displacement at which the crack begins transversing a stiff interface and δ_p is the displacement at the peak force. The enhancement ratio in the work of adhesion $W_{ad,s}/W_{ad,c}$ as a function of $E_s I_s w_s / E_c I_c w_c$ is presented in Figure 5b, where $W_{ad,s}/W_{ad,c}$ increases as $E_s I_s w_s / E_c I_c w_c$ increases. Here, we find $\frac{W_{ad,s}}{W_{ad,c}} \approx \frac{1}{4} \frac{E_s I_s w_s}{E_c I_c w_c}$, which shows that the enhancement in the work of adhesion increases at a slower rate than the enhancement in the force with respect to $E_s I_s w_s / E_c I_c w_c$. This difference in the scaling for force and the work of adhesion provides a mechanism to increase force capacity without expending excess energy during separation. This could be useful for applications such as climbing robots, where adhesive capacity is desirable for supporting loads without large amounts of energy consumption during locomotion.

These results provide guidance for the design and implementation for new classes of adhesive materials. We believe this work will be useful for bandages and wearable electronics, where adhesion to skin can be controlled spatially and directionally. Additionally, as functional kirigami devices find uses in skin-mounted applications, the principles developed here can provide insights into component placement and interfacial structure for controlled and strong adhesion. To highlight this potential, a kirigami-inspired adhesive is mounted on the arm, as shown in Figure 5c. When peeled perpendicular to the cuts, a high resistance to peeling is observed at every compliant-to-stiff interface; however, it is easily peeled off when the cuts are parallel to the peeling direction, as the peel front propagates without meeting a stiff interface, as demonstrated in the anisotropic results in Figure 4. This proof of concept for spatially controlled and anisotropic adhesives demonstrates a path for high-capacity, easy-release dry bandages and wearable devices.

CONCLUSIONS

We have shown that tunable enhanced adhesion and anisotropic adhesion responses can be developed through kirigami-inspired adhesives. The design criteria developed here shows that the force capacity of kirigami-inspired adhesives is controlled by two primary parameters: the difference in bending stiffness $E_s I_s / E_c I_c$ and contact width w_s / w_c and that the length of stiff regions can be utilized to tune adhesion anisotropy. Combined with recent advances in digital manufacturing with subtractive techniques such as laser cutting and additive techniques such as three-dimensional and four-dimensional printing, the concepts and general design criteria

presented in this work provide tools for generating highly controlled adhesive materials. This can enable advanced adhesives and wearable devices with programmed properties for diverse adhesive applications.

EXPERIMENTAL SECTION

Fabrication. PET films (Grainger, $E = 2.6 \pm 0.1$ GPa, $t_{PET} = 125$ μm) are patterned by laser cutting (Epilog Laser Fusion M2, 75 W) and are coated with an adhesive primer (BJB Enterprises SC-5004 silicone primer) on both sides for enhancing the adhesive strength between the PET films and PDMS layers. A thin PDMS elastomer layer (Sylgard 184 with a 20:1 base-to-curing ratio; Dow Corning, $E = 880 \pm 40$ kPa, $t_{PDMS} \approx 300$ μm) is formed on an acrylic sheet using a thin-film applicator (ZUA 2000; Zehntner Testing Instruments) and then precured at 80 °C for 20 min. The prepared PET film is deposited onto the undercured PDMS layer and is then returned to the oven for 100 min for further curing. Another PDMS batch of an identical mixing ratio is cast onto the cured bilayer sample to form a trilayer structure using the same technique. This is cured at 80 °C for 19 h. For model C, PDMS sections in the compliant region are removed by laser cutting.

Mechanical Testing. Samples (PDMS with a 20:1 base-to-curing ratio and PET) are prepared in a dogbone shape, and tests are conducted on an Instron 5944 mechanical testing machine at a constant displacement rate of 1 mm/s. Figure S2a,b presents the stress–strain curves for PDMS and PET dogbone samples, respectively. The elastic modulus is computed as the slope of the linear loading curve.

Characterization. A 90° peel test setup (Universal Grip) is employed to measure peel forces between an adhesive pad and a substrate on an Instron 5944 mechanical testing machine at a constant displacement rate of 1 mm/s. Before each run, the surface of each specimen is cleaned with isopropyl alcohol and Scotch tape to remove all residues. Pressure is applied to the adhesive pad with a roller with a dwell time of 3 min before each test. The interfacial energy $G_c = F_c/w$ is calculated for each specimen by averaging the data points in the plateau compliant region before a peel front meets the first stiff interface.

Bending Rigidity Calculations. For the bending rigidity calculations, we assume that the stiff region and interconnects in the compliant are composed of a single PET strip without considering the two encapsulating PDMS layers, such that $E_s I_s$ is equal to $E_{PET} I_{s,PET}$ and $E_c I_c$ is equal to $E_{PET} I_{c,PET} + E_{PDMS} I_{c,PDMS}$, where $E_{PDMS} I_{c,PDMS}$ is the bending stiffness of the PDMS sections between the interconnects in the compliant regions. We justify the assumption in our particular system as the bending stiffness of PET is approximately equal to that of the entire trilayer ($E_{PET} I_{PET} \approx E_{trilayer} I_{trilayer}$) because of the significantly larger PET modulus compared to PDMS ($E_{PET} \approx 3000 E_{PDMS}$).

ASSOCIATED CONTENT

Ⓢ Supporting Information

The Supporting Information is available free of charge on the ACS Publications website at DOI: 10.1021/acsami.7b18594.

Peel adhesion images and mechanical characterization of materials (PDF)

AUTHOR INFORMATION

Corresponding Author

*E-mail: mbartlet@iastate.edu.

ORCID Ⓞ

Michael D. Bartlett: 0000-0002-7391-5135

Notes

The authors declare no competing financial interest.

■ REFERENCES

(1) Hanakata, P. Z.; Qi, Z.; Campbell, D. K.; Park, H. S. Highly stretchable MoS2 kirigami. *Nanoscale* **2016**, *8*, 458−463.

(2) Sussman, D. M.; Cho, Y.; Castle, T.; Gong, X.; Jung, E.; Yang, S.; Kamien, R. D. Algorithmic lattice kirigami: A route to pluripotent materials. *Proc. Natl. Acad. Sci. U.S.A.* **2015**, *112*, 7449−7453.

(3) Castle, T.; Sussman, D. M.; Tanis, M.; Kamien, R. D. Additive lattice kirigami. *Sci. Adv.* **2016**, *2*, No. e1601258.

(4) Castle, T.; Cho, Y.; Gong, X.; Jung, E.; Sussman, D. M.; Yang, S.; Kamien, R. D. Making the cut: Lattice kirigami rules. *Phys. Rev. Lett.* **2014**, *113*, 245502.

(5) Shyu, T. C.; Damasceno, P. F.; Dodd, P. M.; Lamoureux, A.; Xu, L.; Shlian, M.; Shtein, M.; Glotzer, S. C.; Kotov, N. A. A kirigami approach to engineering elasticity in nanocomposites through patterned defects. *Nat. Mater.* **2015**, *14*, 785−789.

(6) Iwata, Y.; Iwase, E. Stress-Free Stretchable Electronic Device. *2017 IEEE 30th International Conference on Micro Electro Mechanical Systems, MEMS*, 2017; pp 231−234.

(7) Song, Z.; Wang, X.; Lv, C.; An, Y.; Liang, M.; Ma, T.; He, D.; Zheng, Y.-J.; Huang, S.-Q.; Yu, H.; Jiang, H. Kirigami-based stretchable lithium-ion batteries. *Sci. Rep.* **2015**, *5*, 10988.

(8) Someya, T.; Kato, Y.; Sekitani, T.; Iba, S.; Noguchi, Y.; Murase, Y.; Kawaguchi, H.; Sakurai, T. Conformable, flexible, large-area networks of pressure and thermal sensors with organic transistor active matrixes. *Proc. Natl. Acad. Sci. U.S.A.* **2005**, *102*, 12321−12325.

(9) Lamoureux, A.; Lee, K.; Shlian, M.; Forrest, S. R.; Shtein, M. Dynamic kirigami structures for integrated solar tracking. *Nat. Commun.* **2015**, *6*, 8092.

(10) Guo, H.; Yeh, M.-H.; Lai, Y.-C.; Zi, Y.; Wu, C.; Wen, Z.; Hu, C.; Wang, Z. L. All-in-One Shape-Adaptive Self-Charging Power Package for Wearable Electronics. *ACS Nano* **2016**, *10*, 10580−10588.

(11) Yamamoto, Y.; Harada, S.; Yamamoto, D.; Honda, W.; Arie, T.; Akita, S.; Takei, K. Printed multifunctional flexible device with an integrated motion sensor for health care monitoring. *Sci. Adv.* **2016**, *2*, No. e1601473.

(12) Saha, B.; Baek, S.; Lee, J. Highly Sensitive Bendable and Foldable Paper Sensors Based on Reduced Graphene Oxide. *ACS Appl. Mater. Interfaces* **2017**, *9*, 4658−4666.

(13) Kim, D.-H.; Lu, N.; Ma, R.; Kim, Y.-S.; Kim, R.-H.; Wang, S.; Wu, J.; Won, S. M.; Tao, H.; Islam, A.; Yu, K. J.; Kim, T.-i.; Chowdhury, R.; Ying, M.; Xu, L.; Li, M.; Chung, H.-J.; Keum, H.; McCormick, M.; Liu, P.; Zhang, Y.-W.; Omenetto, F. G.; Huang, Y.; Coleman, T.; Rogers, J. A. Epidermal Electronics. *Science* **2011**, *333*, 838−843.

(14) Mahdavi, A.; Ferreira, L.; Sundback, C.; Nichol, J. W.; Chan, E. P.; Carter, D. J. D.; Bettinger, C. J.; Patanavanich, S.; Chignozha, L.; Ben-Joseph, E.; Galakatos, A.; Pryor, H.; Pomerantseva, I.; Masiakos, P. T.; Faquin, W.; Zumbuehl, A.; Hong, S.; Borenstein, J.; Vacanti, J.; Langer, R.; Karp, J. M. A biodegradable and biocompatible gecko-inspired tissue adhesive. *Proc. Natl. Acad. Sci. U.S.A.* **2008**, *105*, 2307−2312.

(15) Baik, S.; Kim, D. W.; Park, Y.; Lee, T.-J.; Ho Bhang, S.; Pang, C. A wet-tolerant adhesive patch inspired by protuberances in suction cups of octopi. *Nature* **2017**, *546*, 396−400.

(16) Kim, S.; Spenko, M.; Trujillo, S.; Heyneman, B.; Santos, D.; Cutkosky, M. R. Smooth Vertical Surface Climbing With Directional Adhesion. *IEEE Trans. Robot.* **2008**, *24*, 65−74.

(17) Hawkes, E. W.; Eason, E. V.; Christensen, D. L.; Cutkosky, M. R. Human climbing with efficiently scaled gecko-inspired dry adhesives. *J. R. Soc., Interface* **2015**, *12*, 20140675.

(18) Bartlett, M. D.; Crosby, A. J. Material Transfer Controlled by Elastomeric Layer Thickness. *Mater. Horiz.* **2014**, *1*, 507−512.

(19) Lee, H.; Um, D.-S.; Lee, Y.; Lim, S.; Kim, H.-j.; Ko, H. Octopus-Inspired Smart Adhesive Pads for Transfer Printing of Semiconducting Nanomembranes. *Adv. Mater.* **2016**, *28*, 7457−7465.

(20) Bartlett, M. D.; Markvicka, E. J.; Majidi, C. Rapid Fabrication of Soft, Multilayered Electronics for Wearable Biomonitoring. *Adv. Funct. Mater.* **2016**, *26*, 8496−8504.

(21) Kim, S.; Wu, J.; Carlson, A.; Jin, S. H.; Kovalsky, A.; Glass, P.; Liu, Z.; Ahmed, N.; Elgan, S. L.; Chen, W.; Ferreira, P. M.; Sitti, M.; Huang, Y.; Rogers, J. A. Microstructured elastomeric surfaces with reversible adhesion and examples of their use in deterministic assembly by transfer printing. *Proc. Natl. Acad. Sci. U.S.A.* **2010**, *107*, 17095−17100.

(22) Autumn, K.; Gravish, N. Gecko adhesion: evolutionary nanotechnology. *Philos. Trans. R. Soc., A* **2008**, *366*, 1575−1590.

(23) Creton, C. Pressure-Sensitive Adhesives: An Introductory Course. *MRS Bull.* **2003**, *28*, 434−439.

(24) Glassmaker, N. J.; Jagota, A.; Hui, C.-Y.; Noderer, W. L.; Chaudhury, M. K. Biologically inspired crack trapping for enhanced adhesion. *Proc. Natl. Acad. Sci. U.S.A.* **2007**, *104*, 10786−10791.

(25) Poulard, C.; Restagno, F.; Weil, R.; Léger, L. Mechanical tuning of adhesion through micro-patterning of elastic surfaces. *Soft Matter* **2011**, *7*, 2543.

(26) Qu, L.; Dai, L.; Stone, M.; Xia, Z.; Wang, Z. L. Carbon Nanotube Arrays with Strong Shear Binding-On and Easy Normal Lifting-Off. *Science* **2008**, *322*, 238−242.

(27) Aksak, B.; Murphy, M. P.; Sitti, M. Adhesion of biologically inspired vertical and angled polymer microfiber arrays. *Langmuir* **2007**, *23*, 3322−3332.

(28) Mengüç, Y.; Yang, S. Y.; Kim, S.; Rogers, J. A.; Sitti, M. Gecko-Inspired Controllable Adhesive Structures Applied to Micromanipulation. *Adv. Funct. Mater.* **2012**, *22*, 1246−1254.

(29) Drotlef, D.-M.; Amjadi, M.; Yunusa, M.; Sitti, M. Bioinspired Composite Microfibers for Skin Adhesion and Signal Amplification of Wearable Sensors. *Adv. Mater.* **2017**, *29*, 1701353.

(30) Kamperman, M.; Kroner, E.; del Campo, A.; McMeeking, R. M.; Arzt, E. Functional Adhesive Surfaces with "Gecko" Effect: The Concept of Contact Splitting. *Adv. Eng. Mater.* **2010**, *12*, 335−348.

(31) Pham, J. T.; Schellenberger, F.; Kappl, M.; Butt, H.-J. From elasticity to capillarity in soft materials indentation. *Phys. Rev. Materials* **2017**, *1*, 015602.

(32) Chung, J. Y.; Chaudhury, M. K. Roles of discontinuities in bio-inspired adhesive pads. *J. R. Soc., Interface* **2005**, *2*, 55−61.

(33) Pendergraph, S. A.; Bartlett, M. D.; Carter, K. R.; Crosby, A. J. Enhancing adhesion of elastomeric composites through facile patterning of surface discontinuities. *ACS Appl. Mater. Interfaces* **2014**, *6*, 6845−6850.

(34) Chan, E. P.; Karp, J. M.; Langer, R. S. A "self-pinning" adhesive based on responsive surface wrinkles. *J. Polym. Sci., Part B: Polym. Phys.* **2011**, *49*, 40−44.

(35) Davis, C. S.; Martina, D.; Creton, C.; Lindner, A.; Crosby, A. J. Enhanced Adhesion of Elastic Materials to Small-Scale Wrinkles. *Langmuir* **2012**, *28*, 14899−14908.

(36) Majumder, A.; Ghatak, A.; Sharma, A. Microfluidic adhesion induced by subsurface microstructures. *Science* **2007**, *318*, 258−261.

(37) Arul, E. P.; Ghatak, A. Control of adhesion via internally pressurized subsurface microchannels. *Langmuir* **2012**, *28*, 4339−4345.

(38) Bartlett, M. D.; Croll, A. B.; King, D. R.; Paret, B. M.; Irschick, D. J.; Crosby, A. J. Looking beyond fibrillar features to scale gecko-like adhesion. *Adv. Mater.* **2012**, *24*, 1078−1083.

(39) King, D. R.; Bartlett, M. D.; Gilman, C. A.; Irschick, D. J.; Crosby, A. J. Creating gecko-like adhesives for "real world" surfaces. *Adv. Mater.* **2014**, *26*, 4345−4351.

(40) Xia, S.; Ponson, L.; Ravichandran, G.; Bhattacharya, K. Toughening and Asymmetry in Peeling of Heterogeneous Adhesives. *Phys. Rev. Lett.* **2012**, *108*, 196101.

(41) Xia, S. M.; Ponson, L.; Ravichandran, G.; Bhattacharya, K. Adhesion of heterogeneous thin films—I: Elastic heterogeneity. *J. Mech. Phys. Solids* **2013**, *61*, 838−851.

(42) Kendall, K. Thin-film peeling-the elastic term. *J. Phys. D: Appl. Phys.* **1975**, *8*, 1449−1452.

(43) Kendall, K. Control of cracks by interfaces in composites. *Proc. R. Soc. London, Ser. A* **1975**, *341*, 409−428.

(44) Dillard, D. A.; Pocius, A. V. *Adhesion Science and Engineering: Surfaces, Chemistry and Applications*; Elsevier, 2002.
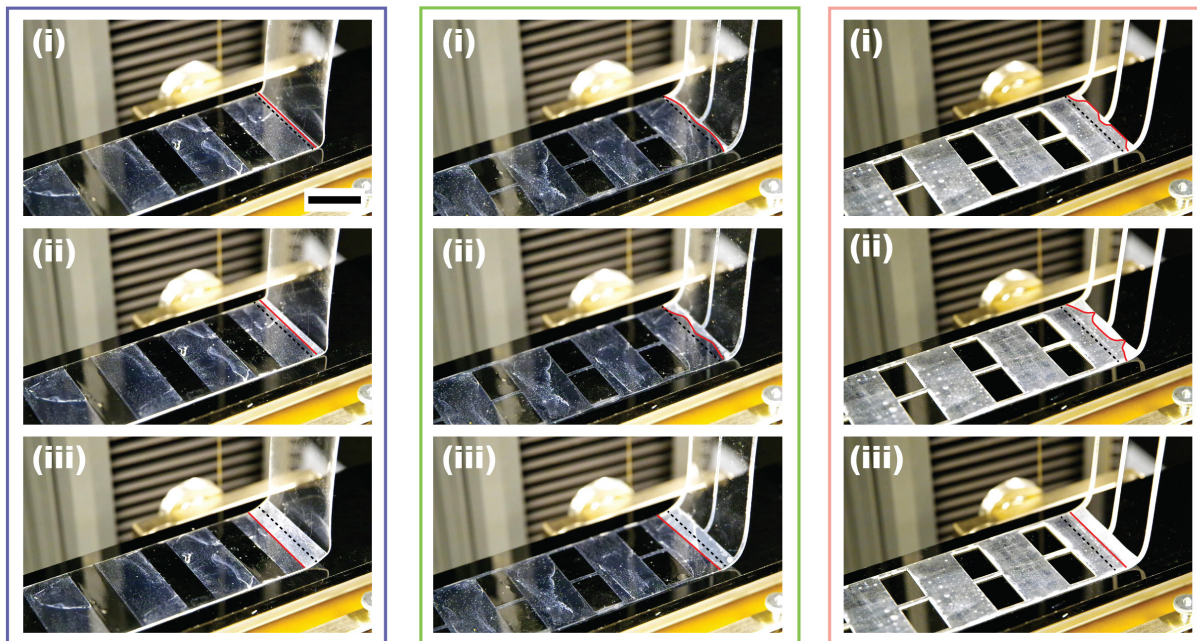
Supporting Information

Kirigami-inspired Structures for Smart Adhesion

Doh-Gyu Hwang, Katie Trent, and Michael D. Bartlett*

Department of Materials Science and Engineering, Soft Materials and Structures Lab, Iowa State University of Science and Technology, 528 Bissell Rd, Ames, IA 50011, USA

E-mail: mbartlet@iastate.edu

Figure S1: Photographs of kirigami-inspired adhesives under a 90° peel test (left column = Model A, center column = Model B, right column = Model C). Red solid lines indicate the position of the peel front and black dashed lines indicate the position of the peel front in a homogeneous adhesive. (Scale bar = 30 mm)
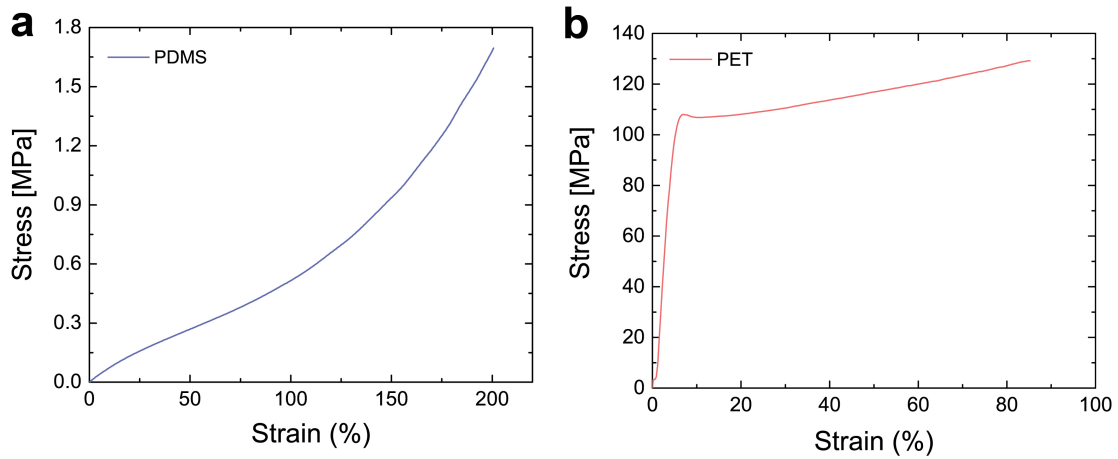
Figure S2. Stress versus strain curve for (a) PDMS with a 20:1 base-to-curing ratio and (b) PET under tensile loading.

Table S1: Tensile modulus, tensile strength and strain at fracture of PDMS and PET dogbone samples.

	E	σ_f	ε_f
PDMS	880 ± 40 kPa	1.6 ± 0.4 MPa	202.0 ± 1.7 %
PET	2.6 ± 0.1 GPa	130.2 ± 1.3 MPa	90.5 ± 6.8 %